ORIGINAL PAPER

Somatic *Braf*^{V600E} mutation in the cerebral endothelium induces brain arteriovenous malformations

Tianqi Tu[1] · Jiaxing Yu[1] · Chendan Jiang[1] · Shikun Zhang[1] · Jingwei Li[1] · Jian Ren[1] · Shiju Zhang[1] · Yuan Zhou[1] · Ziwei Cui[1] · Haohan Lu[1] · Xiaosheng Meng[1] · Zhanjing Wang[2] · Dong Xing[3,4] · Hongqi Zhang[1] · Tao Hong[1]

Abstract

Current treatments of brain arteriovenous malformation (BAVM) are associated with considerable risks and at times incomplete efficacy. Therefore, a clinically consistent animal model of BAVM is urgently needed to investigate its underlying biological mechanisms and develop innovative treatment strategies. Notably, existing mouse models have limited utility due to heterogenous and untypical phenotypes of AVM lesions. Here we developed a novel mouse model of sporadic BAVM that is consistent with clinical manifestations in humans. Mice with *Braf*^{V600E} mutations in brain ECs developed BAVM closely resembled that of human lesions. This strategy successfully induced BAVMs in mice across different age groups and within various brain regions. Pathological features of BAVM were primarily dilated blood vessels with reduced vascular wall stability, accompanied by spontaneous hemorrhage and neuroinflammation. Single-cell sequencing revealed differentially expressed genes that were related to the cytoskeleton, cell motility, and intercellular junctions. Early administration of Dabrafenib was found to be effective in slowing the progression of BAVMs; however, its efficacy in treating established BAVM lesions remained uncertain. Taken together, our proposed approach successfully induced BAVM that closely resembled human BAVM lesions in mice, rendering the model suitable for investigating the pathogenesis of BAVM and assessing potential therapeutic strategies.

Keywords Brain arteriovenous malformation · *Braf* · Somatic mutation · Endothelial cell · Stereotaxic injection · Mouse model

Tianqi Tu, Jiaxing Yu and Chendan Jiang contributed equally to this work.

✉ Jiaxing Yu
xwyujiaxing@163.com

✉ Hongqi Zhang
xwzhanghq@163.com

✉ Tao Hong
hongtao.edu@gmail.com

1 Department of Neurosurgery, Xuanwu Hospital, China International Neuroscience Institute, Capital Medical University, 45 Changchun St, Beijing 100053, China

2 Medical Imaging laboratory of Core Facility Center, Capital Medical University, Beijing 100054, China

3 Biomedical Pioneering Innovation Center (BIOPIC), School of Life Sciences, Peking University, Beijing, China

4 Beijing Advanced Innovation Center for Genomics (ICG), Peking University, Beijing, China

Introduction

Brain arteriovenous malformations (BAVMs) are high-flow vascular anomalies characterized by pathological shunts between arteries and veins [1, 2]. The associated robust blood flow, in conjunction with the dysplastic nature of the vessel wall, renders BAVM a significant cause of hemorrhagic stroke, particularly among young people [3]. Current therapeutic approaches for BAVMs primarily rely on surgical resection, endovascular embolization, and stereotactic radiosurgery. However, in cases where malformed vessels extensively affect eloquent cerebral regions, the efficacy and safety of such invasive treatments may be inadequate [4]. Consequently, the development of novel treatment strategies, particularly pharmacologic therapies, has emerged as an urgent clinical need [5].

However, the absence of an animal model that faithfully recapitulates the human BAVMs has impeded further preclinical investigation into these complex lesions.

Previous studies predominantly focused on vascular malformation models caused by pathogenic genes associated with hereditary hemorrhagic telangiectasia (HHT) [6–8]. However, the representation of models based on HHT genes may be limited due to their distinct genetic background in comparison to sporadic BAVM, as HHT patients only constitute 2-3% of the BAVM cohort [9, 10]. Since 2018, a series of studies have consistently reported a high prevalence of *KRAS/BRAF/MAP2K1* somatic mutations in surgical sporadic AVM samples, thereby offering a promising avenue for comprehensive investigation into the underlying biological mechanisms of the disease [2, 11, 12]. By crossbreeding gene-modified mice (lox-stop-lox *Kras* conditional mouse strain) and inducible brain endothelial cell drivers (*Slco1c1-CreER* mouse strain), the first *KRAS* mutation-related BAVM mouse model was induced by Jason E Fish and colleagues [13]. Another contributing study conducted by Park ES and colleagues induced a BAVM model by intravenously injecting AAV-BR1-CAG-*KRAS* ^{G12V} into wild-type C57BL/6 mice [14]. These encouraging studies have provided us with new insights into the etiology of AVMs. However, similar to conventional HHT-based models of BAVM, the strategies employed for generating animal models through systematic induction of pathogenic gene expression have inherent practical limitations in terms of random distribution and heterogeneous phenotypic manifestations of lesions [15]. Meanwhile, although somatic *BRAF* activating mutations have been identified in both intracranial and extracranial AVMs, no preclinical studies have yet investigated whether the presence of an active *BRAF* mutation alone is sufficient to drive AVM formation.

To address the aforementioned issues, we developed a novel mouse model of sporadic BAVM by locally inducing the *Braf* ^{V600E} mutation in cerebral endothelial cells. We found that the pathological features of the *Braf* ^{V600E} mutation-induced BAVM model included luminal dilation, disrupted stability of the vascular wall, intracerebral hemorrhage, and an active inflammatory microenvironment. Through single-cell sequencing, we found that differential gene expression that influenced endothelial cell shape maintenance, movement, intracellular transportation and intercellular junction stability may contribute to BAVM formation. We also observed a significant difference in the therapeutic effectiveness of Dabrafenib on BAVMs in their initial stages compared to those that were established. Collectively, the present study established a novel and clinically consistent mouse model for sporadic BAVMs, which is suitable for elucidating potential mechanisms and exploring innovative treatment approaches.

Materials and methods

Animals

All experiments involving mice were performed following the approved protocols of the Institutional Animal Care and Use Committee (IACUC) at the Chinese Institute for Brain Research, Beijing. C57BL/6JSmoc-*Braf* $^{em1(flox-V600E)Smoc}$ was purchased from Shanghai Model Organisms Center, Inc (Shanghai, China) [16]. The animals were housed in a temperature- and humidity-controlled facility with a 12-hour light/12-hour dark cycle. They were provided with access to food and water freely. To conduct a more precise investigation on the impact of elevated *Braf* ^{V600E} mutation in the cerebrovasculature, we obtained heterozygous mice of the C57BL/6JSmoc-*Braf* $^{em1(flox-V600E)Smoc}$ strain (*Braf* $^{flox/+}$) and subsequently subjected them to self-fertilization. This breeding strategy yielded offspring with homozygous (*Braf* $^{flox/flox}$), heterozygous (*Braf* $^{fl/+}$), and wild-type (*Braf* $^{+/+}$) mice (In the text, "flox" was abbreviated as "fl.").

Adenoassociated virus injection

AAV-BR1-CAG-*Cre*-WPRE-SV40pA was obtained from Guangzhou PackGene Biotechnology Co.,Ltd (Guangzhou, China). Each mouse in different subgroups were administered with 100nl of sterile PBS containing 2×10^{10} genome copies [GC] of AAV by stereotactical injection as described previously [17]. In brief, mice were induced with 5% isoflurane and maintained under 2% isoflurane anesthesia. They were then securely positioned in a specially designed stereotaxic apparatus for stereotactic injection (RWD Life Science Co., Ltd.,). For the injection procedure, the following coordinates relative to bregma were utilized: lateral ventricle, anteroposterior −0.1,5 mm, mediolateral −0.75 mm, and dorsoventral from the skull surface −2.0 mm. To prevent the backflow of the injection vehicle, the microelectrode was kept in place for 6 min after the injection was completed. Once the electrode was fully retracted, the scalp was sutured and re-disinfected to avoid infection. The animals were placed on a heating pad until they fully recovered from the surgery and were then returned to their respective cages.

Magnetic resonance imaging (MRI) evaluation

The MRI procedure was carried out using a 7.0 Tesla small animal MRI scanner (Bruker, Germany). T2-weighted magnetic resonance imaging (MRI) and magnetic resonance angiography (MRA) were conducted to assess the BAVM lesions. Paravision 5.1 software (Bruker BioSpin) was used as the user interface, along with a Linux PC running Topspin 2.0, to control the MRI scanner and analyze the

acquired data. To anesthetize the mice, a combination of 5% isoflurane and 95% oxygen was administered in a plexiglass chamber for induction. Once inside the MRI scanner, a mixture of 2% isoflurane and 98% oxygen was used for maintenance of anesthesia in the center of the magnetic field. Respiratory rate of the mice throughout the scanning process was closely monitored by the animal physiological monitoring system. 3D Slicer (version 5.2.2, www.slicer.org) and ImageJ2/Fiji software (version 2.1.0, National Institutes of Health, USA) were utilized for image analysis and visualization.

Craniotomy survival surgery

A chronic cranial window was created following previously established procedures [17, 18]. Briefly, mice were anesthetized using isoflurane (5% for induction, 2% for maintenance) and securely placed in a custom-made stereotaxic apparatus. During the procedure, mice were placed on a heating pad covered with a cotton pad to maintain a body temperature. Ophthalmic lubricant was applied to the eyes to prevent dryness, and the depth of anesthesia was regularly monitored. After securing the head, the hair on the scalp was removed using Nair. Subsequently, the scalp was cleaned and disinfected with 75% ethanol and iodine solution at least three times. To fully expose the skull, we made a midline incision on the scalp and gently removed the periosteum using blunt forceps. A craniotomy window (3–4 mm in diameter) was then performed to expose the somatosensory cortex by using a dental drill. Upon the completion of intraparenchymal AAV injection, gelatin sponges were used for hemostasis. A sterile cap, equipped with a custom-made titanium ring, as well as a custom-made head plate, were sealed on the cranial window securely using cyanoacrylate adhesive and dental cement. Dexamethasone (100 µl, 1 mg/ml in physiological saline) was administered via intraperitoneal injection prior to the surgery, and ceftriaxone sodium (100 µl, 0.1 g/ml in physiological saline) was intraperitoneally injected within three days post-surgery. The entire surgical procedure was conducted under sterile conditions. The mice were individually housed in separate cages after AAV injection and cranial window creation, and they were monitored and imaged for a period of 42 days before they were harvested.

Two-photon live imaging

The procedures for in vivo imaging were conducted as previously reported [18, 19]. The mice with a custom-made head plate were placed on a custom microscope stage, allowing imaging to be performed while the mice remained conscious. FITC-dextran dye (2000 kDa, Sigma) at a dose of 100 µl (1% w/v, saline) was administered via retro-orbital injection to visualize the vasculature and blood flow. An upright two-photon laser scanning microscope (TPLSM, FVMPE-RS, Olympus) with galvanometric scanners was used to observe the cerebral vasculature. The imaging system was controlled by software (F31S-SW, Olympus) and equipped with a Mai Tai HP Ti: Sapphire laser (InSight X3TM, Spectra Physics). A 25 × 1.05 NA water immersion objective lens (Olympus) captured images at a resolution of 1024 × 1024 pixels. The optimal excitation wavelength for FITC was set to 960 nm, and a non-scanning GaAsp detector (Olympus) was used to detect the fluorescence emitted by FITC. Additionally, an emission bandpass filter (BA495-540, green) was employed to select a specific wavelength range of the fluorescence signal. X-T line scanning was performed over a range of 10–50 µm for 2000 cycles to measure the velocity of red blood cells in each capillary, and Z-stack images were acquired with a step size of 2 µm and a depth of 400 µm. The acquired data was reconstructed and analyzed by using ImageJ2/Fiji software (version 2.1.0, National Institutes of Health, USA).

Latex perfusion and clearing process

Blue latex was injected into the left ventricle and the specimens were fixed in 10% formalin for 24 h. Subsequently, the specimens were dehydrated in a gradient of methanol (50%, 75%, 90%, and 100% each for 24 h). Finally, they were cleared in a 1:1 mixture of benzyl benzoate and benzyl alcohol. The images were captured under a microscope (Zeiss SteREO Discovery, V12) using Zen version 3.6 software.

H&E staining and prussian blue staining

The euthanized mice underwent a series of processing steps, first being flushed with PBS (pH = 7.4) solution, followed by treatment with a 4% (w/v) paraformaldehyde (PFA) solution. The brain tissue was collected and embedded in paraffin, and then sliced into sections of 5–10 µm thickness. The sections were stained with hematoxylin and eosin (H&E staining), and Prussian Blue.

Immunofluorescence staining

The tissue was fixed in 4% formaldehyde for 24 h, followed by gradient dehydration in 20% and 30% sucrose solutions for 12 h each. Following that, the tissue was embedded in optimal cutting temperature compound (OCT compound) and sectioned with a thickness of 40 µm. The following antibodies were used: primary, anti-CD31 (1:50, BD Biosciences, 550,274), anti-Ki67 (1:500, abcam, ab15580), anti-iba1 (1:500, abcam, ab178846), anti-Cxcl10 (1:500,

ThermoFisher, #701,225); Secondary, Alexa Fluor™ 488 (1:500; ThermoFisher, #A-11,006), Alexa Fluor™ 546 (1:500; ThermoFisher, #A-11,035) and Alexa Fluor™ 647 (1:500; ThermoFisher, #A-21,247 and #A-31,573). Then the sections were mounted using an anti-fade mounting medium containing DAPI (S2110, Solarbio).

EdU staining

For the study of EdU cell proliferation staining, the EdU Cell Proliferation Kit with Alexa Fluor 555 (C0075L, Beyotime) was utilized. After receiving the AAV injection, the mice were intraperitoneally administered EdU (6 mg/kg body weight) once every day. In brief, after completing a 10-minute fixation with 4% paraformaldehyde and a subsequent 10-minute permeabilization using 0.3% Triton X-100 (T8200, Solarbio), tissue sections are ready for the subsequent steps of EdU staining, including EdU incubation, termination of the reaction, as well as the following visualization and analysis processes.

Western blot

Immunoblot analysis was performed using the general procedure described earlier [20]. Based on the results of the MRI scan, tissue samples containing the lesions were accurately collected. After preparing whole-cell lysates using RIPA buffer (89,901, Thermo Fisher Scientific), the protein concentration was determined using a BCA Protein Assay kit (P0012, Beyotime). An equal quantity of total protein (20 μg) was loaded for western blot analysis. The antibodies employed in this study were as follows: p-ERK1/2 (1:1000, CST, #9101), t-ERK (1:1000, CST, #9102), p-MEK (1:1000, CST, #2338), t-MEK (1:1000, CST, #4694), BRAF-V600E (1:500, Abcepta, AP22342b), Tubulin (1:1000, CST, #2148). Secondary antibodies were Anti-mouse IgG (1:1000, CST, #7076) and Anti-rabbit IgG, Antibody (1:1000, CST, #7074).

RT-qPCR

Total mRNA was extracted (00266, Shanghai Yuduo Biotechnology Co., Ltd. Shanghai, China, 00266) and cDNA was synthesized using a commercial kit (KR118-02, Tiangen Biotech, Co., Ltd. Beijing, China). Real-time PCR Kit (AQ131-01, FullGold, Beijing, China) was used for the quantitative reverse transcription polymerase chain reaction. The following primers were used:

GAPDH (forward-5' GGTGAAGGTCGGTGTGAAC G, reverse-5' CTCGCTCCTGGAAGATGGTG), MMP2 (forward-5' TGTTCAACGGTCGGGAATAC, reverse-5' GTAAACAAGGCTTCATGGGG), MMP9 (forward-5' C

TTCAGAAGCAGCTCTCCCTC, reverse-5' ATGATGGT CCCACTTGAGG), IL-1β (forward-5' AGCTACCTGTG TCTTTCCCGC, reverse-5' CTTTCAGCTCATATGGGTC C), TNF-α (forward-5' CCACGCTCTTCTGTCTACTGC, reverse-5' CCTTGAAGAGAACCTGGGAG), IL-6 (forward-5' ATACCACTCCCAACAGACCTGC, reverse-5' T TCAATAGGCAAATTTCCTGA). The PCR data were analyzed using software Applied Biosystems™ 7500 Fast Real-Time PCR System.

Drug administration

Dabrafenib (in 0.5% HPMC and 0.2% Tween 80 in H$_2$O) was administered orally via daily gavage at a dose of 30 mg/kg, and the control group received an equivalent volume of vehicle solution without Dabrafenib [21]. In this experiment, we implemented two strategies for drug administration. The first strategy involved initiating drug treatment on the first day following the AAV injection, while the second strategy began drug administration two weeks after modeling. The treatment was performed for 6 days out of every 7-day week. Continuous magnetic resonance imaging was performed to monitor changes in the lesions. Neurological and behavioral scoring were conducted during the sixth week, followed by tissue harvesting.

Neurological function and behavioral score

All data were recorded by two independent experimenters blindly.

Wire hanging test

Mice were subjected to a wire hanging test, where they were placed on a 2 mm gauge wire suspended 30 cm above a soft bedding layer. The mice were allowed to hang on the wire for a duration of 3 min or until they fell. In cases where mice fell, they were repositioned on the wire up to 5 times within the 3-minute trial.

Rotarod test

During each trial, mice were positioned on a 4.5 cm diameter horizontal rotating rod. They were allowed to run on the rod at a speed of 4 rpm for up to 5 min. Up to three trials were conducted per day.

Beam balance

The scoring method used for the beam balance assessment was based on the previously established protocol [22], which was used to assess the ability of mice to walk on a circular

wooden beam within 1 min. The walking ability was evaluated based on consecutive three trials, and the average score was calculated by summing the scores (ranging from 0 to 4) obtained in each trial.

Gait balance test

Gait assessment was performed according to the documentation in the literature [23]. Before experiment, the animals were trained in a closed box, encouraging them to move towards a target box at the end of the corridor. Each mouse underwent two training sessions until they freely ran to the target box without any encouragement. During the testing phase, the animals' paws were coated with non-toxic ink (red ink was used for the front paws, and blue ink for the hind paws). Subsequently, these animals were placed in a transparent corridor apparatus (65 cm x 5 cm x 15 cm) lined with a pre-cut sheet of white paper. As they ran from the near end to the enclosed target box at the other end of the apparatus, relevant footprints were left on the paper at the bottom of the apparatus. To provide gait measurements, the paper print was analyzed to determine the stride length and width for both the front and hind paws of each animal.

Seizure video record and EEG monitoring

The methods described in the literature were used for electrode placement and brain EEG monitoring [24]. Video monitoring was conducted for 8 h each day over a continuous period of 5 days. Electroencephalogram (EEG) monitoring was also performed on mice experiencing epileptic seizures to capture any abnormal brain wave activity associated with the seizures. The grading of seizures in mice follows the Racine's standard five-stage scale: Stage I: Immobility and staring. Stage II: Stiff posture. Stage III: Repetitive movements and head nodding. Stage IV: Forelimb clonus and rearing. Stage V: Severe tonic-clonic seizures [25].

Brian tissue collection

Experiments were performed on mice 6-week after AAV injection. The mice were euthanized and perfused with ice-cold PBS (P.H = 7.4). The brains were then surgically removed and placed in ice-cold Dulbecco's modified Eagle medium (DMEM, Gibco) supplemented with 1x penicillin/streptomycin (Thermo Fisher Scientific, Cat#15,140,122). The unilateral brain tissue containing the BAVM lesions (excluding the olfactory bulb and cerebellum) was skillfully and accurately dissected for the preparation of single-cell suspension. The subsequent preparation of single-cell samples was performed using the Adult Brain Dissociation Kit (Miltenyi Biotec B.V. & Co. KG, Order no. 130-107-677).

The experiment was conducted strictly following the detailed steps outlined in the instruction manual.

Singlecell RNA sequencing and data processing

Sequencing data processing

Raw gene expression matrices were generated for each sample by the Cell Ranger (Version 6.1.2) Pipeline coupled with mouse reference version refdata-gex-mm10-2020-A. The output filtered gene expression matrices were analyzed by R software (Version 4.1.2) with the Seurat package (Version 4.3.0). All samples were merged into one Seurat object using the merge function in Seurat. Data were filtered for cells (nfeatures > 200) and mitochondrial genes (percent_mito < 10%).

Dimension reduction, unsupervised clustering and cell-type annotation

Dimension reduction and unsupervised clustering were performed according to the standard workflow in Seurat. NormalizeData and FindVariableFeatures functions were applied to normalize and find highly variable genes (hvgs) within the single nucleus gene expression data, respectively. Then, the effect of the percentage of mitochondrial gene count was regressed out by using the ScaleData function with the parameter "vars.to.regress='percent.mt'". A principal component analysis (PCA) matrix was calculated to reduce noise by using RunPCA, and twenty-seven principal components were selected for downstream analysis. Then Uniform Manifold Approximation and Projection (UMAP) and clustering were performed to identify clusters. Cluster specific genes were detected using the FindAllMarkers function with default parameters. The main cell types were annotated based on the expression pattern of differentially expressed genes (DEGs) and the well-known cellular markers from the literature.

To identify subpopulations within Endothelial, we use a dataset from the literature (https://doi.org/10.1016/j.cell.2020.01.015) as the reference dataset, and followed the tutorial (https://satijalab.org/seurat/articles/multimodal_reference_mapping.html) to map each donor dataset from the query individually. We used the FindTransferAnchors function with normalization. method = "SCT" and MapQuery function with reference. reduction = "pca".

Differential expression analysis

To identify differentially expressed genes between different clusters, we used FindAllMarkers function to perform differential gene expression analysis. Marker genes detected in

> 25% cells in a cluster with average log-fold-change > 0.25 were used in the analysis. We also used single-sample GSEA (ssGSEA), which calculates each dataset's scores we are interested.

Trajectory inference

Trajectory analysis was performed with Monocle2 (version 2.22.0) to determine the dramatic transitional relationships among cell types and clusters. Raw count data from the SeuratObject was converted to a CellDataSet object using the import CDS function in monocle2. Genes that were differentially expressed between subpopulations were set as the ordering genes. The minimum spanning tree was constructed using the reduceDimensions function (reduction_method = "DDRTree").

Data analysis and statistics

All statistical analysis were performed using GraphPad Prism Software (Version 8.2.0). Numerical data were presented as median ± SEM. Normal distribution was determined using *Shapiro-Wilk normality* test and/ or *Kolmogorov-Smirnov normality*. For normally distributed data, two-tailed unpaired Student's *t* test and One-way ANOVA followed by Tukey's multiple comparison test were used and *Mann-Whitney* test of non-parametric analysis was used for non-normally distributed data. *Fischer's exact* test was used to compare the incidence rate of BAVM among different groups. *Kaplan-Meier plot* was used to analyze the survival rate of mice in different groups and followed by *Log-rank* test to determine the difference in survival rate between groups. Two-sided $P < 0.05$ was considered statistically significant and are denoted as follows: *$P < 0.05$; **$P < 0.01$; ***$P < 0.001$.

Results

Induction of a brain EC-specific *Braf*^{V600E} mutation promotes BAVM lesions in mice that resemble those in humans

We initially attempted to induce BAVM formation through intravenous injection of AAV-BR1-*Cre* into mice with a *Braf*$^{LSL-V600E}$ (*Braf*$^{+/+}$, *Braf*$^{fl/+}$ and *Braf*$^{fl/fl}$) genetic background (Supplementary Fig. 1a). However, all mice with the homozygous background (*Braf*$^{fl/fl}$) died within three weeks after induction (10/10), while the mortality rate of mice with the heterozygous background (*Braf*$^{fl/+}$) reached 80% (8/10) within six weeks after induction (Supplementary Fig. 1b). Furthermore, the MR images and pathological

tests only revealed scattered hemorrhages without any observed BAVM lesions (Supplementary Fig. 1c-e). Examination of the major organs through anatomical dissections (Supplementary Fig. 1f) did not reveal any discernible factors that could account for the exceptionally high mortality rate observed.

Consequently, we optimized our strategy to precisely deliver AAV-BR1-*Cre* via stereotactic injection into the specific brain region of adult (P42) mice (Fig. 1a). During the six-week period following AAV injection, *Braf*$^{+/+}$ (wild-type) mice exhibited 100% survival, while the survival rates in the *Braf*$^{fl/+}$ and *Braf*$^{fl/fl}$ groups of mice were 70% (7/10) and 30% (3/10), respectively (Fig. 1b). To investigate the success of this strategy in inducing mouse BAVM formation, we employed blue latex perfusion (Fig. 1c) and 3D reconstruction of MR angiography (MRA) (Fig. 1d) to visualize the entire brain vasculature 6 weeks after AAV-BR1-*Cre* injection. We found that both *Braf*$^{fl/fl}$ and *Braf*$^{fl/+}$ mice exhibited typical BAVM lesions. Remarkably, the angioarchitecture of the mouse BAVMs closely resembled that of human lesions, as the feeding arteries, nidus with arteriovenous shunts, and draining veins could be clearly identified in both latex perfusion and MRA images (Fig. 1c and d). To investigate the BAVM formation over time, we conducted sequential MR scans at weeks 2, 4, and 6 following AAV injection in a cohort of mice with *Braf*$^{fl/fl}$, *Braf*$^{fl/+}$ or *Braf*$^{+/+}$ genetic backgrounds ($n = 10$ for each group). In the *Braf*$^{+/+}$ mice, MRI images indicated only a self-limiting edema signal in the AAV injection sites (Fig. 1e). The BAVMs of *Braf*$^{fl/+}$ mice demonstrated a chronic progressive pattern, with a prevalence of 50% (4/8) at week two, reaching 100% (7/7) by week four (Fig. 1e-g). In the *Braf*$^{fl/fl}$ group, BAVMs were observed in 100% of the mice (4/4, 6 mice died within 2 weeks) at week two (Fig. 1e-g). Meanwhile, compared to *Braf*$^{fl/fl}$ mice, *Braf*$^{fl/+}$ mice exhibited a significantly smaller lesion volume at sixth week after AAV injection (Fig. 1h). These data suggested that BAVM model in *Braf*$^{fl/+}$ mice was a suitable choice for preclinical investigations requiring prolonged observation.

The occurrence of spontaneous obliteration or substantial growth in human BAVMs is rare [26]. To ascertain the concordance of the model's long-term natural progression with human BAVMs, we established a cohort of mice for long-term observation ($n = 7$). Consistent with other groups, the mortality rate was (3/7), with the majority occurring before 6th weeks. The remaining 4 mice were observed for six months (26 weeks) after AAV injection. One of them experienced new intracerebral hemorrhage accompanied by seizures, while the lesions of the remained 3 mice progressed slowly (Supplementary Fig. 2a -c).

To ascertain whether BAVMs in the mouse model could mimic the ability of human BAVMs to affect any cerebral
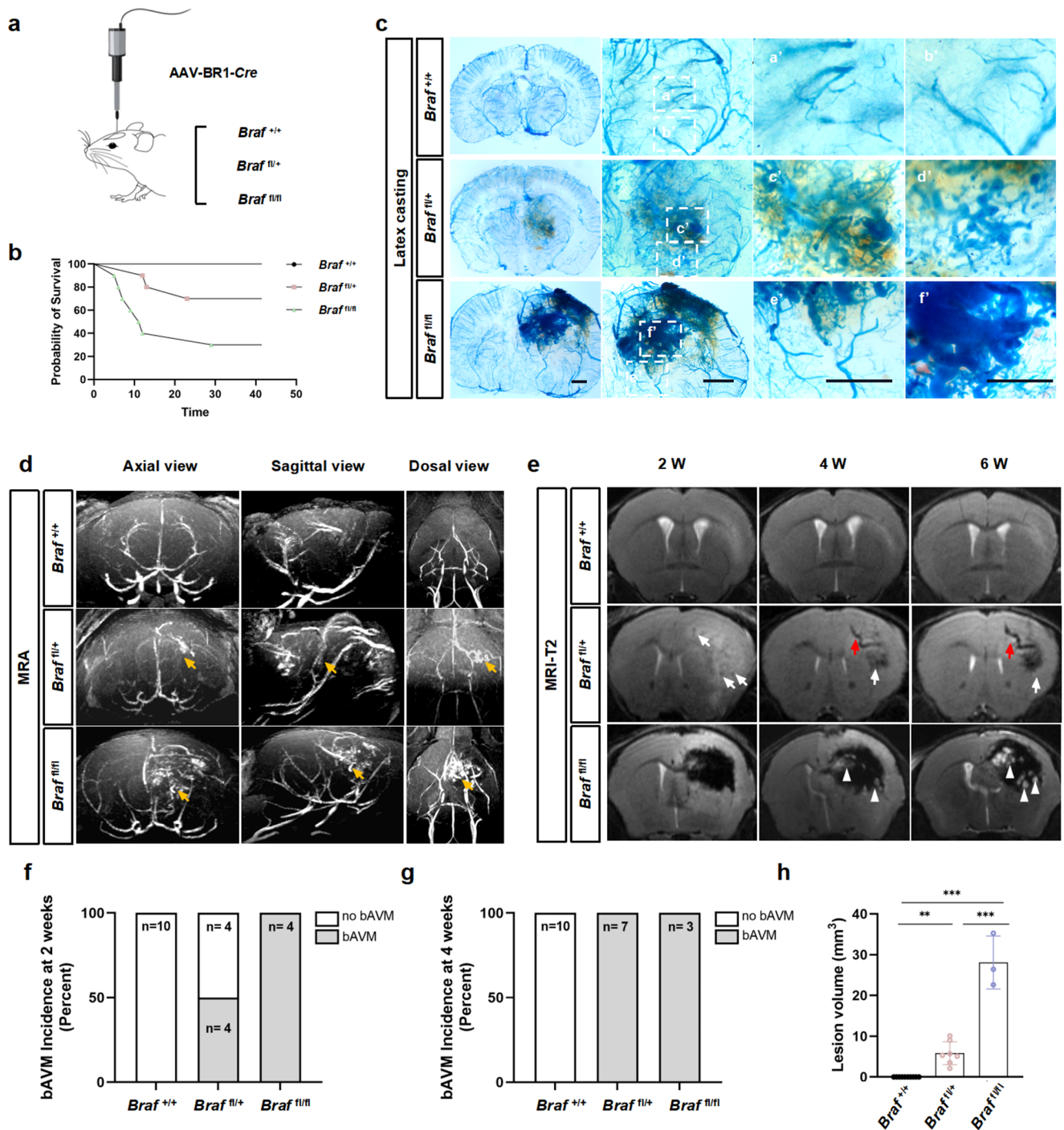
Fig. 1 The $Braf^{V600E}$ mutation in cerebral ECs could induce the formation of BAVM in mice. (**a**) Schematic of stereotactic injection of AAV-BR1-*Cre* to the brains of mice with $Braf^{+/+}$, $Braf^{fl/+}$ and $Braf^{fl/fl}$ backgrounds. (**b**) Survival curves of each group of mice within six weeks after induction (n = 10 in each group). *Log-rank* test. (**c**) Representative images of latex-casted clarified brains at 6th week after AAV-BR1-*Cre* injection. Images of (**a'**) to (**f'**) were locally magnified images. Panels (**a'**) and (**b'**) depicted the normal brain vasculature, while panels (**c'** to **f'**) showed the feeding arteries and draining veins connected to the nidus. Scale bar = 1 mm for each panel. (**d**) Representative images of TOF-MRA for mice in different groups at 6th week after injection of AAV-BR1-*Cre*. The yellow arrows pointed to tangled vasculatures along arterial vessels. (**e**) Representative images of T2 MRI for mice in different groups at 2nd, 4th, and 6th week after injection of AAV-BR1-*Cre*. The white arrows represented the hemorrhagic lesions, and the red arrows indicate typical flow void signals. The white arrowheads indicated newly developed hemorrhagic lesions. (**f**) Statistical analysis was conducted on the lesion formation rates for each group of mice during the 2nd week. *Fisher's exact* test. (**g**) Statistical analysis of lesion formation rates in each group of mice at the 4th week. *Fisher's exact* test. (**h**) Statistical analysis of lesion volume in each group of mice at the sixth week post-induction. (n = 10 for $Braf^{+/+}$ group, n = 7 for $Braf^{fl/+}$ group and n = 3 for $Braf^{fl/fl}$ group). one-way ANOVA

region and age, we induced BAVMs in multiple murine brain regions and at various ages in $Braf^{fl/+}$ mice. MRI at the fourth week after induction confirmed that the current approach achieved a 100% success rate in inducing BAVM formation in the striatum, parietal cortex, and cerebellum (Supplementary Fig. 2a, b, d and e). Furthermore, we confirmed that BAVM lesions could also be induced at all developmental stages in mice (including P1, P7, P14, P21, P90 and P180) (Supplementary Fig. 2f-k).

To test whether the model could reproduce typical symptoms (focal neurological deficits and seizures) of BAVM in patients, we conducted the Wire Hanging Test, the Rotarod Test, the Beam Balance Test, Gait assessment and electroencephalography (EEG) monitoring. Compared to $Braf^{+/+}$ mice, $Braf^{fl/+}$ and $Braf^{fl/fl}$ BAVM model mice exhibited a significantly higher frequency of falls or reduced wire traversal time, lower scores in the Beam Balance Test, decreased running duration on the rotarod, and impaired gaits as indicated by a narrower stride width and shorter stride length (Supplementary Fig. 3a-g). Furthermore, EEG captured seizures in the $Braf^{fl/+}$ BAVM model (Supplementary Fig. 3h and i).

Taken together, these findings demonstrated that stereotactic AAV-BR1-*Cre* injection into the brains of mice with a $Braf^{fl/fl}$ or $Braf^{fl/+}$ genetic background effectively induced sporadic BAVM, which exhibited remarkable clinical resemblance to human BAVM. Meanwhile, the chronic progression of BAVMs in $Braf^{fl/+}$ mice demonstrated their enhanced ability to mimic lesions in humans and made the model more suitable for preclinical investigations.

$Braf^{V600E}$-induced BAVMs are mainly formed through dilation of preexisting microvasculature

We used the transparent cranial window technique to comprehensively monitor the real-time progress of sporadic BAVM formation (Fig. 2a). After injecting AAV-BR1-*Cre* into the cortical region beneath the window, daily imaging with stereomicroscopy showed that the $Braf^{fl/+}$ and $Braf^{fl/fl}$ mice exhibited a progressive emergence of vascular abnormalities characterized by dilated vessels and spontaneous hemorrhage (Fig. 2b). Two-photon microscopy further captured the progressive dilation of normal blood vessels during the observation (Fig. 2c, d and f). The analysis of red blood cell velocity indicated an increased blood flow velocity, suggesting changes in the hemodynamics of the BAVM (Fig. 2e and g). Additionally, Evans blue dye (EBD) leakage was observed under in vivo imaging, indicating the disruption of the blood–brain barrier within the BAVM lesions (Fig. 2h). Taken together, these data demonstrated that the BAVMs were mainly formed through the dilation of preexisting microvasculature. Additionally, our results also

Fig. 2 The development of BAVMs caused by $Braf^{V600E}$ mutation ▶ could be observed by in vivo imaging. (**a**) Schematic representation of real-time live imaging of the brain vasculature in a mouse with a cranial window. (**b**) Representative images of the development of AVM lesions in the mouse brain. Scale bar = 500 μm for each panel. (**c**) Z-stack images taken by a two-photon laser excitation microscope depicted the development process of BAVM in mice. Green, FITC-dextran. Scale bar = 100 μm for each panel. (**d** and **f**) Analysis of the changes in blood vessel diameter within the BAVM lesion indicated that initially normal blood vessels undergo gradual dilation over time ($n = 12$ from 3 mice). *Paired t test.* (**e** and **g**) The velocity of blood cells shown in the vessels was measured through line scanning, and the analysis of red blood cell velocity indicated an increase in blood flow speed. The data was obtained from images plotted using X-T mode (X-axis shows T in the images) ($n = 12$ from 3 mice). *Paired t test.* (**h**) In vivo two-photon imaging showed Evans Blue Dye (EBD) leakage around BAVMs. Cyan, Evans Blue Dye. Scale bar = 100 μm for each panel

highlighted the potency of employing a local transparent skull window as a reliable strategy for real-time monitoring of BAVM progression.

Decreased vascular wall stability, partial endothelial proliferation and neuroinflammation are the pathological features of $Braf^{V600E}$-induced BAVMs

Previous research has revealed that the key pathological features of BAVM include luminal dilation and decreased vascular wall stability [27–31]. Our results further depicted the pathological structure of the dilated blood vessels (Fig. 3a). In the BAVM samples from the $Braf^{fl/+}$ and $Braf^{fl/fl}$ groups, we observed irregular vascular morphology with significant capillary dilation (Fig. 3a). Furthermore, the capillary basement membranes became thinner with blurred boundaries. The endothelial cells also exhibited irregular morphology, accompanied by indistinct tight junctions and cytoplasmic structures (Fig. 3a). H&E staining of brain sections confirmed significant vascular dilations in both the $Braf^{fl/+}$ and $Braf^{fl/fl}$ groups (Fig. 3b), and Prussian blue staining revealed bleeding and hemosiderin deposition around these lesions (Fig. 3c).

To determine whether the $Braf^{V600E}$ mutation would initiate BAVM formation via excessive endothelial proliferation, we conducted Ki67 staining and EdU staining (Fig. 3d to i). In the dilated vessels of the BAVM, the proportion of endothelial cells within the lesion's vascular lumen that were Ki67-positive did not exceed 20% (Fig. 3d, f and g). Meanwhile, the proportion of EdU-positive endothelial cells did not exceed 10% (Fig. 3e, h and i). These results suggested that although endothelial proliferation could be implicated in the pathogenesis of BAVM, it may not be the sole cause of vascular dilation.

Perivascular accumulation of microglia/macrophages and elevated levels of inflammatory markers is another common pathological phenomenon in BAVMs [14, 32, 33].
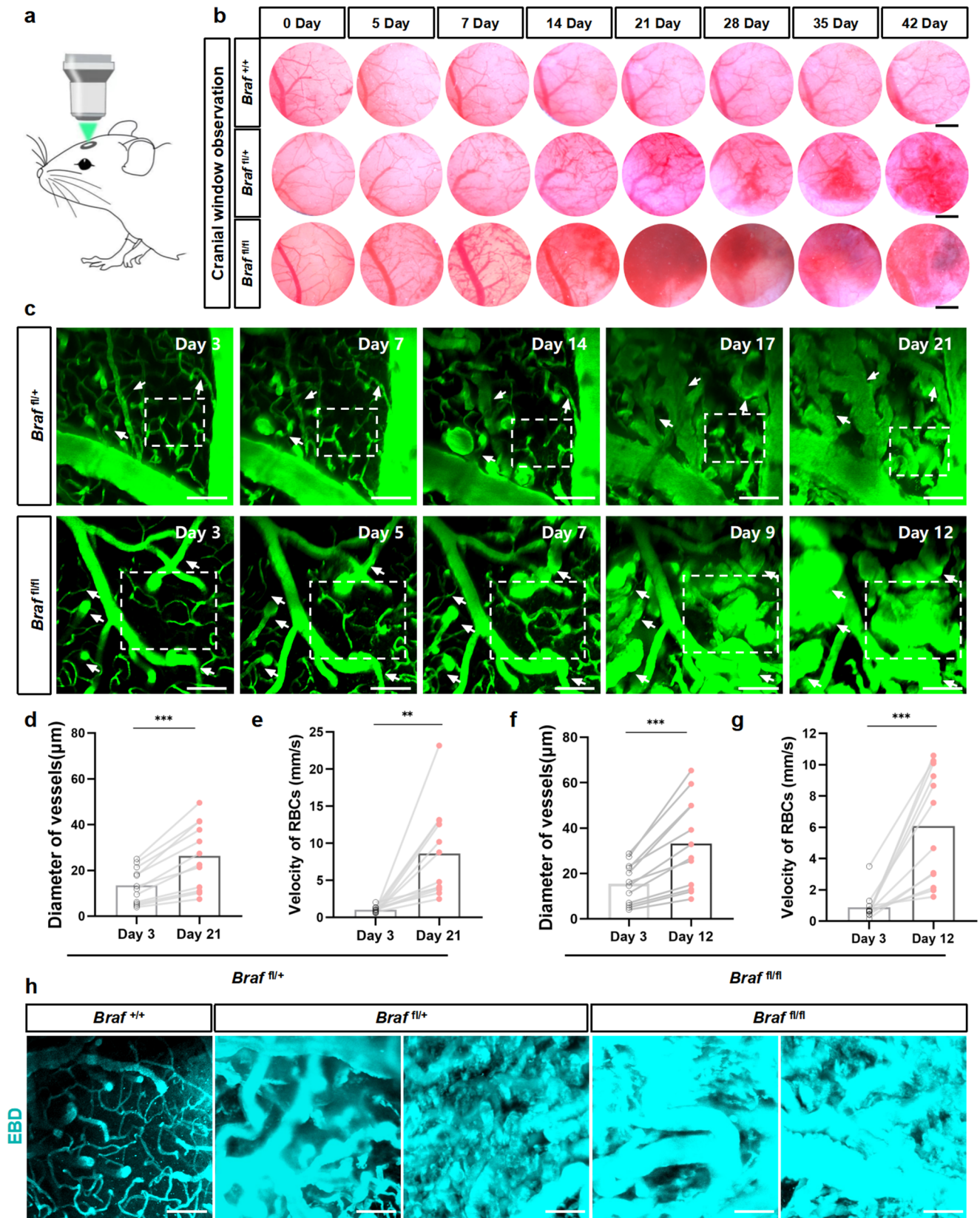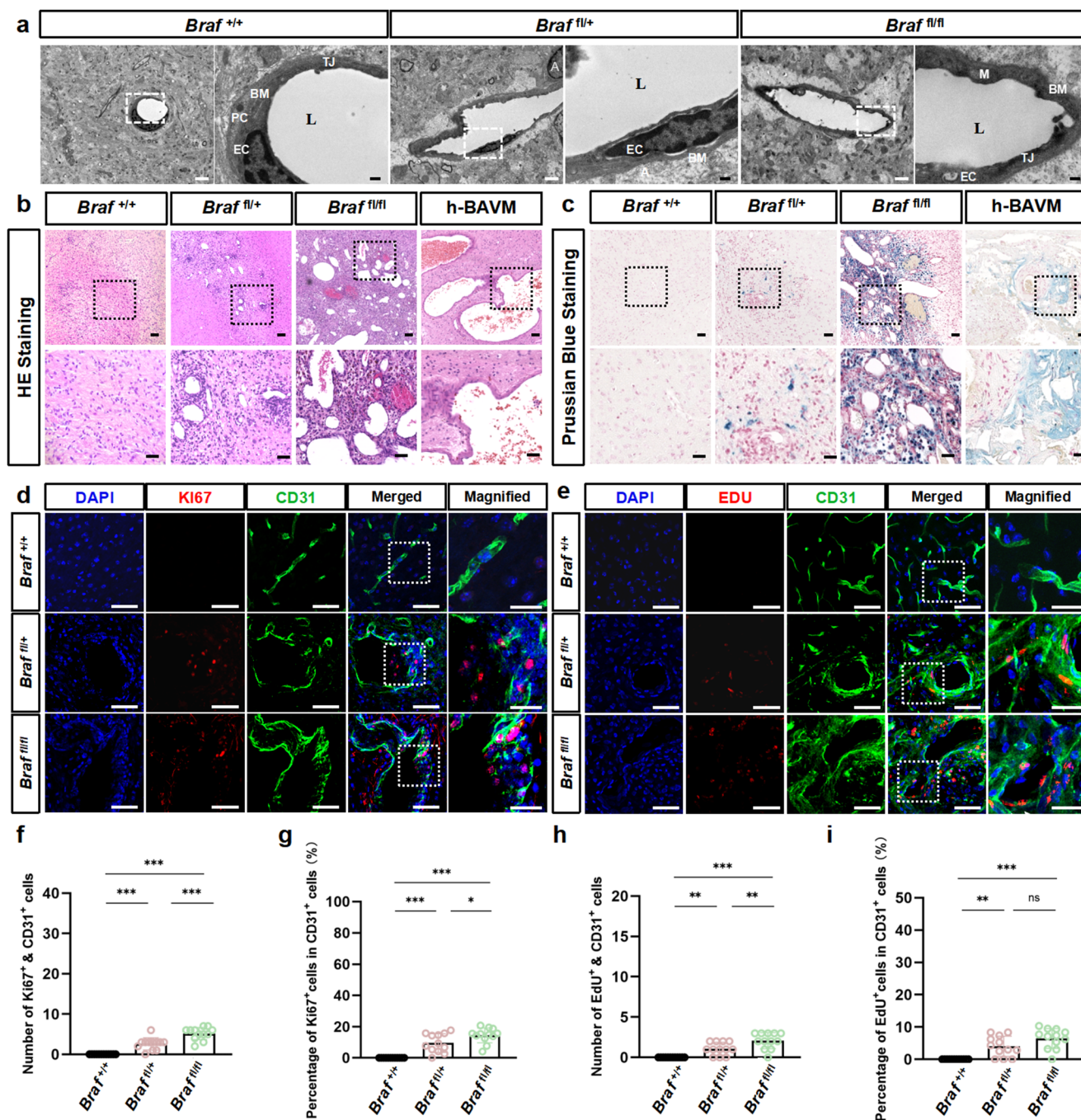
Fig. 3 The BAVM lesions induced by $Braf^{V600E}$-mutation in the endothelium of mice exhibit pathological features akin to human AVM. (**a**) Transmission electron microscopy (TEM) showed the ultrastructure of the BAVM. Blood vessel basement membrane (BM), Endothelial cells (EC), Astrocytes (A), Pericytes (PC), Cytoplasmic mitochondria (M), Tight junctions (TJ) and Lumen (L). Scale bar $=2$ μm for the left panel of each group (the white bar), and Scale bar $=500$ nm for the right panel of each group (the black bar). (**b**) Representative images of Hematoxylin and eosin (H&E) stained sections exhibited hemorrhage and dilated lumens. Scale bar $=100$ μm for the upper panel of each group, and Scale bar $=50$ μm for the lower panel of each group. (**c**) Representative images of Prussian blue staining revealed the presence of hemorrhage and hemosiderin deposits around the lesion. Scale bar $=100$ μm for the upper panel of each group, and Scale bar $=50$ μm for the lower panel of each group. (**d** and **e**) Representative images of BAVM proliferation marker staining (Ki67 and EdU, respectively). Scale bar $=20$ μm for the magnified panels, and scale bar $=50$ μm for the rest of the panels. (**f** and **h**) The quantification of the number of Ki67$^+$ and EdU$^+$ cells co-localized with CD31$^+$ cells, respectively ($n=12$ slices from 3 mice). one-way ANOVA. (**g**) The statistical analysis was performed on the proportion of Ki67$^+$ cells co-localized with CD31$^+$ cells in relation to the total number of CD31$^+$ cells within a single field of view ($n=12$ slices from 3 mice). one-way ANOVA. (**i**) The statistical analysis was conducted for the proportion of EdU$^+$ cells co-localized with CD31$^+$ cells relative to the total number of CD31$^+$ cells within a single field of view ($n=12$ slices from 3 mice). one-way ANOVA

In our model, we observed a significant accumulation of activated microglia/macrophages surrounding the vascular walls within the lesions (Fig. 4a to c). In addition, in the BAVM tissues, we noticed a significant upregulation of various inflammatory factors, including tumor necrosis factor-α (TNF-α), interleukin-1 beta (IL-1β), interleukin-6 (IL-6), matrix metalloproteinase-2 (MMP-2), and MMP-9 (Fig. 4d-h).

Collectively, these results demonstrated typical pathological features of BAVM in $Braf^{V600E}$-induced models, including disrupted vascular wall stability, vascular dilations, focal intracranial hemorrhage, and inflammatory microenvironment.

Single-cell sequencing reveals the heterogeneity of the pathological endothelium in $Braf^{V600E}$-induced BAVMs

To explore the potential mechanisms of how mutated endothelial cells form BAVM, we performed single-cell sequencing of brain tissues from the lesion site in the disease group ($Braf^{fl/+}$) and the corresponding site in the control group ($Braf^{+/+}$) (Fig. 5a). Using dimensionality reduction and clustering analysis on the single-cell data, we identified 16 cell clusters in the brain tissue, including endothelial cells, immune cells, astrocytes, neurons, and other cell types (Fig. 5b and c). By projecting the endothelial cell population to previous atlas data, we further identified nine subgroups: large artery, artery, capillary arterial, capillary, capillary venous, large vein, interferon, choroid plexus and artery shear stress (Fig. 5d and e) [34].
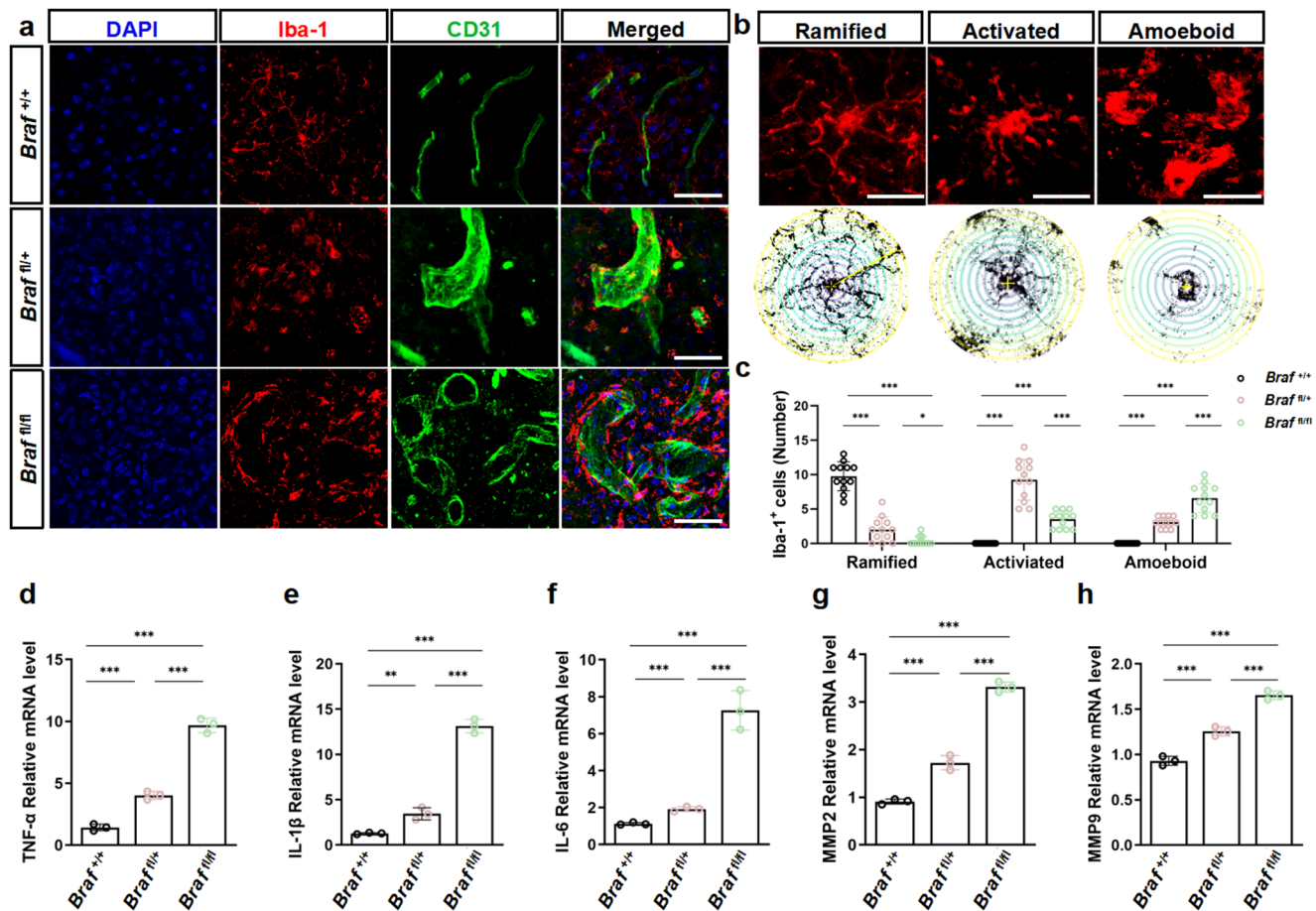

Fig. 4 Inflammatory cells and markers are increased in $Braf^{V600E}$-induced BAVMs. (a) Representative images of Anti-Iba-1 immunofluorescence staining showed that Iba-1+ cells are distributed around BAVMs. Scale bar = 50 μm. (b) The representative morphology of Iba-1+ cells. Using ImageJ-Sholl analysis, the measurement of the maximum radius of the cell soma and the radius extending beyond the longest branch of the cells was conducted to assess the morphology of Iba-1 + microglia/macrophages. Scale bar = 20 μm. (c) The quantification of number of Iba-1+ cells with different functional states (n = 12 slices from 3 mice). one-way ANOVA. (d to h) displayed the mRNA levels of TNF-α, IL-1β, IL-6, MMP-2 and MMP-9 in BAVM lesions from $Braf^{+/+}$, $Braf^{fl/+}$ and $Braf^{fl/fl}$ mice (n = 3 tissues). one-way ANOVA

Fig. 5 Single-cell sequencing reveals cellular aberrations in the mouse BAVM lesions. (**a**) Schematic of isolation and cell sampling from mouse brain ($n=3$ mice, respectively). (**b**) Dot plot showed expression of cell markers in cell clusters. Oligodendrocyte progenitor cells (OPC). (**c**) UMAP visualization showed cell types from mouse brain of $Braf^{+/+}$ and $Braf^{fl/+}$ groups. (**d** and **e**) UMAP visualization of endothelial cells (ECs) from mouse brain of $Braf^{+/+}$ and $Braf^{fl/+}$ groups via UMAP projection. (**f**) Correlation matrix of gene expression profiles of cerebrovascular endothelial cell states between $Braf^{+/+}$ and $Braf^{fl/+}$ groups. The horizontal axis represented self-measured data, the vertical axis represented reference data, and the correlation was calculated using Pearson correlation coefficient. (**g**) The stacked bar chart showed the proportion of different subtypes of endothelial cell states

We observed significant differences between the *Braf*^{+/+} group and *Braf*^{fl/+} group in the correlation matrix of gene expression profiles in various endothelial cell subpopulations (Fig. 5f). Furthermore, in addition to the classical endothelial cell phenotypes (artery, capillary, and vein ECs), a distinct endothelial cell type, interferon ECs, was identified in the disease group with a greatly increased cell proportion (Fig. 5g). The interferon ECs were mainly characterized with genes that were associated with the immune response, antiviral defense and inflammation regulation, such as *Bst2, Ifitm3, Isgl5, Ifit3* and *Cxcl10* (Fig. 6a) [35–44]. Immunostaining of pathological tissue sections with the representative marker *CXCL10* confirmed the colocalization of these cells with BAVM ECs (Fig. 6b and c). Pseudotime analysis revealed that interferon ECs may originate from capillary venous cells (Fig. 6d). To identify genes that were specific to the interferon ECs in the diseased group, we performed the gene set variation analysis (GSVA) between the *Braf*^{+/+} and *Braf*^{fl/+} groups. We observed a significant upregulation of several genes, including *Actg1, Arpc4, Arpc5, Actn1, Atcb, Actr2*, and *Actr3*, in the *Braf*^{fl/+} group (Fig. 6e and g). These genes are closely related to cell shape maintenance, cell movement, intracellular transport, cell adhesion, and cell–cell interactions [45–47]. We also found significant downregulation of genes related to cell–cell adhesion and cell membrane integrity, such as *Tns1, Tns2, Zo-2, Magi3*, and *Ocln*, in the *Braf*^{fl/+} group (Fig. 6f and g) [48–54]. Taken together, our single-cell data offered a valuable resource into the etiology of BAVM formation.

Inhibition of *Braf*[V600E] can impede the formation of BAVMs, but fails to rescue established BAVMs

We evaluated the therapeutic efficacy of Dabrafenib, an *FDA*-approved *Braf*[V600E] inhibitor, at different developmental stages of the *Braf*^{fl/+} BAVM models. We initiated treatment from the first day after AAV injection and continued the medication for six weeks (Fig. 7a). Three out of seven mice died in the vehicle group, while no mouse died in the Dabrafenib treatment group (Fig. 7b). There were no significant changes in body weight in either group over the course of six weeks (Fig. 7c). At the sixth week after induction, MRI showed that the lesion volume in the treatment group was significantly smaller than that in the vehicle group (Fig. 7d and f). And in the 3D reconstruction of MRA, the nidus was nearly imperceptible (Fig. 7e), indicating a notable inhibition of BAVM formation and progression by Dabrafenib. By using stereomicroscopy and two-photon microscopy, we observed that the lesion growth (Fig. 7g) and the vascular leakage (Fig. 7h) were prevented by Dabrafenib. Furthermore, we also noticed that treatment with Dabrafenib improved the neurological and behavioral functions of mice (Supplementary Fig. 4a-g). The improvement could be attributed to consequent alleviation of neuronal damage (Supplementary Fig. 4h and i). The Western blotting results indicated that Dabrafenib's action might be attributed to the inhibition of *Braf*[V600E], consequently suppressing the activity of p-MEK and p-ERK (Fig. 7i-l).

However, the formation of BAVM lesions typically occurs early in a patient's life, hence AVM lesions are already fully developed prior to clinical treatment. To test the effectiveness of Dabrafenib in this circumstance, we initiated Dabrafenib treatment two weeks after AAV induction (Fig. 8a). In the subsequent four weeks of Dabrafenib treatment, 2 out of 6 mice died in vehicle group (33.33%) and 3 out of 7 died in Dabrafenib group (42.86%) (Fig. 8b). The body weight change did not exhibit any statistically significant difference between the two groups of mice (Fig. 8c). Notably, the MRI results obtained at the fourth week after Dabrafenib/Vehicle treatment also did not show any statistically significant differences in the lesion volume between the two groups (Fig. 8d-f). These results collectively revealed that early intervention with Dabrafenib effectively inhibited the activation of the MEK/ERK pathway, thereby suppressing the growth of BAVMs in mice; however, the drug may not be as effective for established BAVMs.

Discussion

In this study, we established a mouse model of BAVM caused by *Braf*[V600E] mutation in brain endothelial cells for the first time. The vascular architecture, biological behaviors, and pathological features of the lesions in this model exhibited a favorable resemblance to those observed in human BAVMs. In addition, this model, with the ability to precisely control the dosage and injection site of AAV, demonstrated a notable advantage in achieving a high degree of uniformity in BAVM phenotypes, encompassing lesion size, severity of hemorrhage, and lesion location. These characteristics make our BAVM model a valuable platform for preclinical research on sporadic BAVMs.

As a pioneering effort to establish a somatic *Braf*[V600E] mutation-induced BAVM model, we tried to induce BAVM formation in mice with both homozygous (*Braf*^{fl/fl}) or heterozygous (*Braf*^{fl/+}) mutations. Notably, although BAVMs were successfully induced in both groups, the BAVMs in the *Braf*^{fl/fl} background mice exhibited a more aggressive phenotype, characterized by a significantly large nidus with rapid progression, intense spontaneous hemorrhage and higher mortality. In contrast, BAVMs in *Braf*^{fl/+} background mice typically exhibited a disease course resembling that of human lesions, characterized by a less aggressive growth progression and lower hemorrhage rate. Additionally,
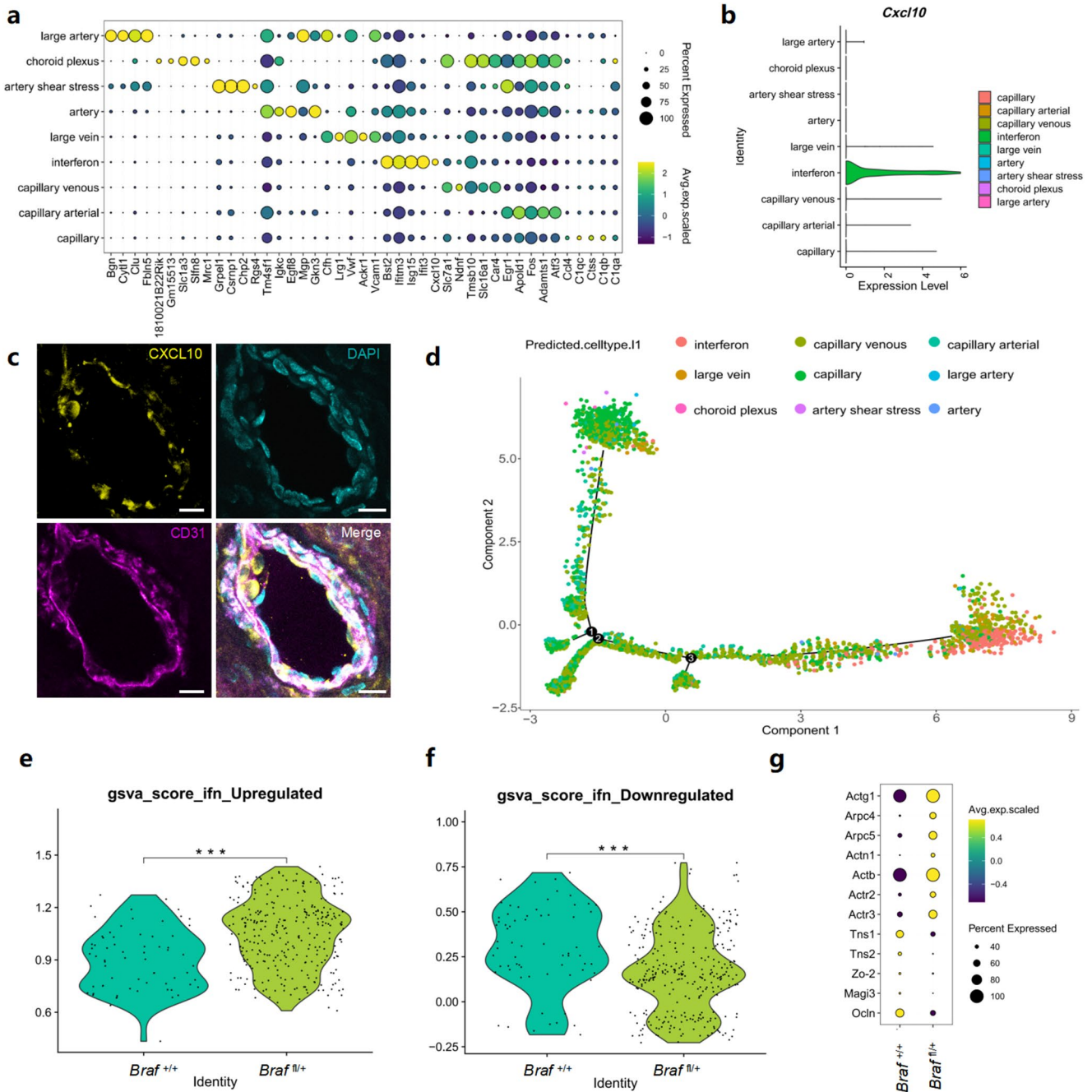
Fig. 6 The differential expression gene (DEGs) of the lesion-associated endothelium in malformed cerebrovasculature partially explains the pathogenesis of the BAVM. (**a**) Dot plot showed expression of endothelial cell state markers. (**b**) Violin plot of *CXCL10* expression showed specificity to BAVM of *Braf*$^{fl/+}$ groups. (**c**) Representative confocal microscopy images demonstrated the expression of CXCL10 (yellow) within CD31$^+$ endothelial cells (magenta) in the BAVM nidus. Scale bar = 10 μm for each panel. (**d**) Pseudotime analysis of endothelial cells by Monocle2. (**e**) Gene set variation analysis of cellular cytoskeleton regulatory function related genes in interferon ECs of *Braf*$^{+/+}$ and *Braf*$^{fl/+}$ groups. (ifn = interferon). (**f**) Gene set enrichment analysis of cellular tight junction and cell stability related genes in interferon ECs of *Braf*$^{+/+}$ and *Braf*$^{fl/+}$ groups. Student's *t* test. (**g**) Dot plot showing differential gene expression (DEG) for markers related to crucial cell function mentioned in (**e** and **f**)
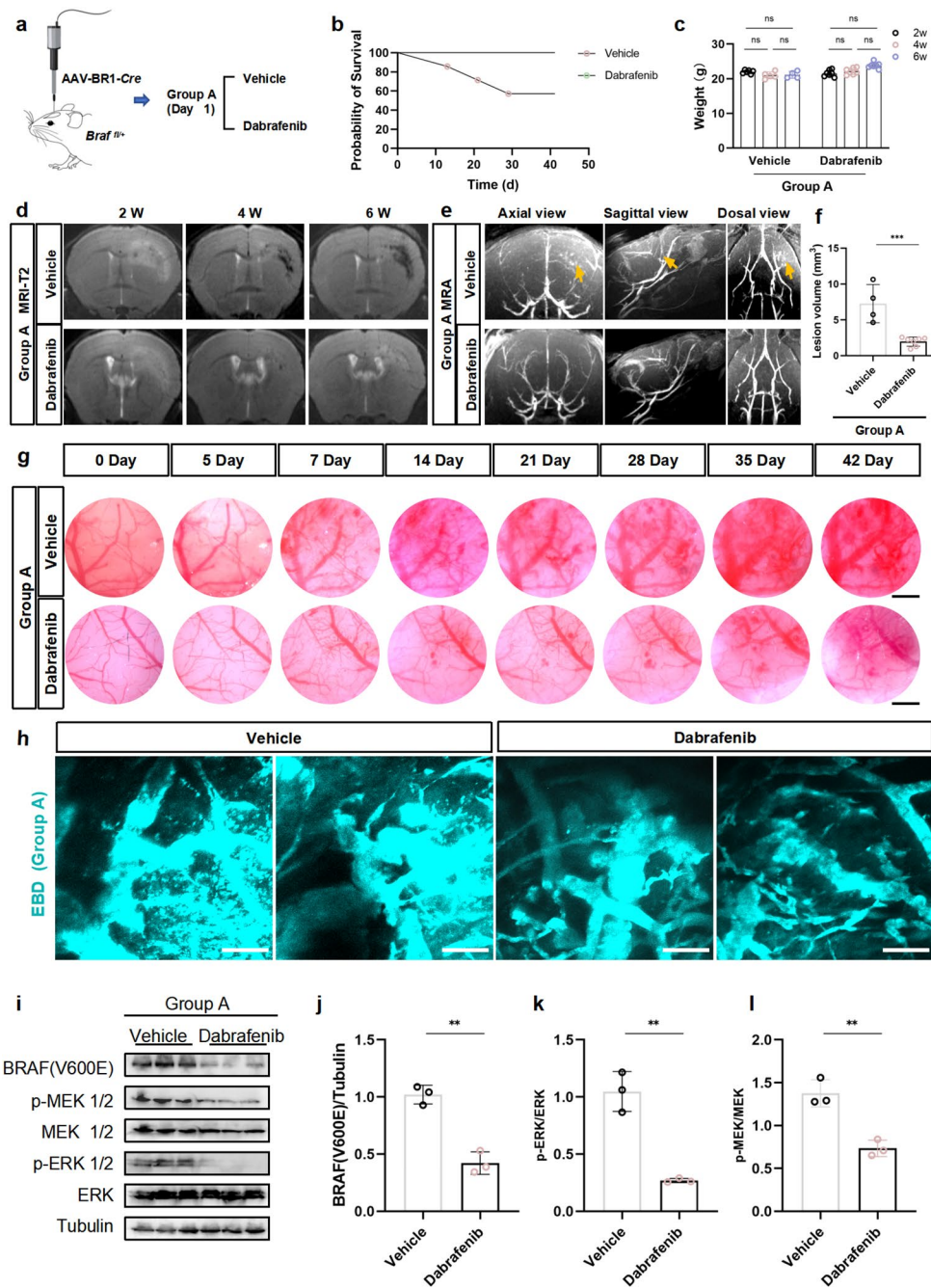
Fig. 7 Early administration of $Braf^{V600E}$ inhibitor prevents the formation and progression of $Braf^{V600E}$-mediated BAVM. (**a**) Schematic of Dabrafenib treatment strategies. In Group A, the mice were treated with Dabrafenib and control solvents (vehicle) from the 1st day after AAV-BR1-*Cre* induction. (**b**) Survival curves of each group of mice within six weeks after induction ($n=7$ in each group). *Log-rank* test. (**c**) Records of body weight changes in each group of mice within six weeks after induction. one-way ANOVA. (**d**) Representative images of T2 MRI of mice in Group A at 2nd, 4th, and 6th week after injection of AAV-BR1-*Cre*. The white arrows represented the hemorrhagic lesions, and the red arrows indicated typical flow void signals. (**e**) Representative images of TOF-MRA of mice in Group A at 6th week after injection of AAV-BR1-*Cre*. The yellow arrows pointed to tangled vascula-

tures along arterial vessels. (**f**) Statistical analysis of lesion volume in mice of Group A at the 6th week post-induction ($n=4$ in vehicle group and (n)=7 in Dabrafenib group). Student's t test. (**g**) Representative images of the BAVM development process in mouse brain. Observations were made continuously from the day of AAV injection until the 42nd day (6th week). Scale bar $=500$ μm. (**h**) Representative images demonstrated that the EBD leakage was alleviated in the Dabrafenib group compared to the vehicle group. Cyan, Evans Blue Dye. Scale bar $=100$ μm for each panel. (**i**) Western blot images of signaling molecules in BAVM tissue from vehicle group and Dabrafenib group. (**j, k** and **l**) The quantification of BRAF(V600E)/Tubulin, p-MEK/MEK and p-ERK/ERK. ($n=3$ mice). Student's t test
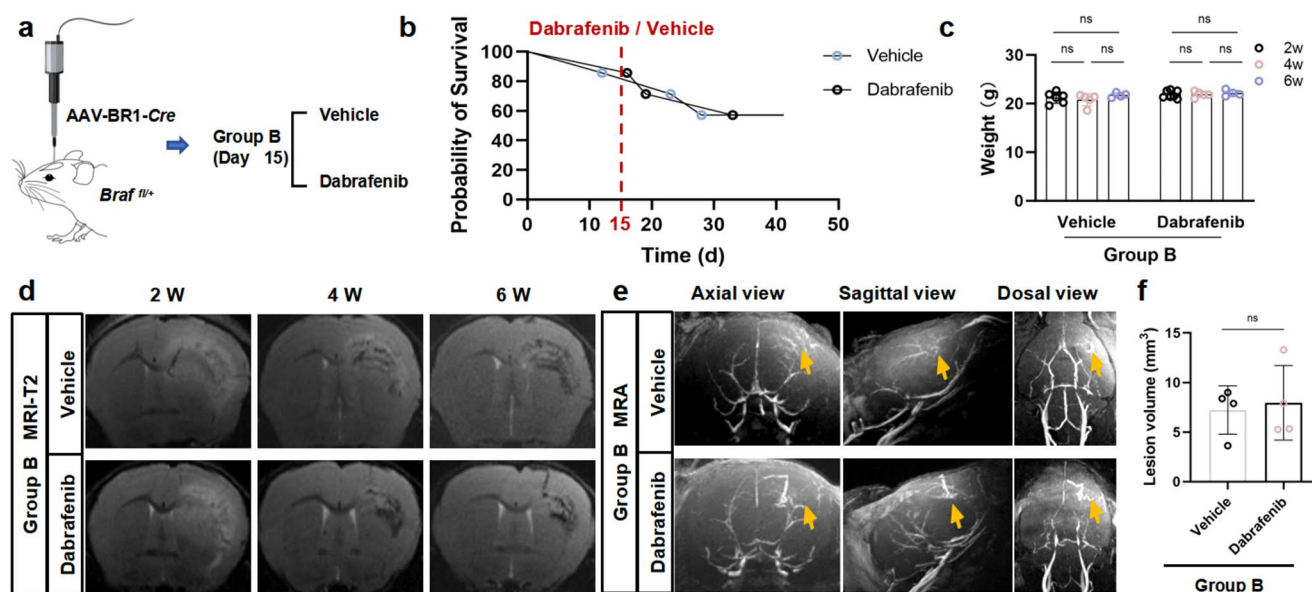
Fig. 8 Late-stage Dabrafenib treatment cannot reverse the formation of $Braf^{V600E}$ mediated BAVM.(**a**) Schematic of Dabrafenib treatment strategies. In the Group B, the mice were treated with Dabrafenib and control solvents (vehicle) from the 15th day after AAV-BR1-*Cre* induction. (**b**) Survival curves of each group of mice within six weeks after induction ($n = 7$ in each group). *Log-rank* test. (**c**) Records of body weight changes in each group of mice within six weeks after induction. one-way ANOVA. (**d**) Representative images of T2 MRI of mice in Group B at 2nd, 4th, and 6th week after injection of AAV-BR1-*Cre*. (**e**) Representative images of TOF-MRA of mice in Group B at 6th week after injection of AAV-BR1-*Cre*. The yellow arrows pointed to tangled vasculatures along arterial vessels. (**f**) Statistical analysis of lesion volume in mice of Group B at the 6th week post-induction ($n = 4$ in vehicle group and Dabrafenib group). Student's *t* test

chronic neurological deficits and seizures were also replicated in the heterozygous models. The extended progression of heterozygosity ensured the feasibility of symptom recording and assessment, therefore rendering the model well suited for experiments requiring prolonged observation, such as investigating disease development and new treatment methods for sporadic BAVMs.

Arteriovenous shunt represents the fundamental characteristic of BAVMs [55, 56]; however, the underlying mechanism remains elusive. Considering the pivotal mitogenic role of the MAPK pathway in diverse epithelial cells and the elevated expression level of VEGF in both human and mouse BAVM samples, it is reasonable to hypothesize that *KRAS/BRAF* mutations would elicit robust proliferation of endothelial cells, subsequently resulting in a robust pathological angiogenesis [57, 58]. Surprisingly, our two-photon microscopy through a transparent skull window provided evidence supporting the dilation of preexisting microvasculature rather than angiogenesis during the pathogenesis of BAVMs. This finding was consistent with the observation by Murphy et al. that AVMs arose from enlargement of capillaries in an active Notch4 (Notch4*)-mediated AVM model [59]. In addition, the relatively moderate positive rate of Ki67/EdU staining in our study also suggested that endothelial proliferation may not be the primary cause of the pathogenesis of BAVMs.

To investigate the potential pathological mechanisms underlying vessel dilation and acquire a more comprehensive understanding of lesion formation, we conducted single-cell sequencing analysis on the BAVM lesion tissue. In a specific subtype of endothelial cell population, interferon ECs, that was closely associated with AVM formation, we observed a significant upregulation of genes related to cell cytoskeleton synthesis and metabolism, such as *Actg1, Arpc4, Arpc5, Actn1, Atcb, Actr2,* and *Actr3*. These gene subsets may participate in the regulation of cellular migration and morphogenesis, thereby contributing to vascular dilation [45–47]. Conversely, we identified *Tns1, Tns2, Zo-2, Magi3,* and *Ocln* among the significantly downregulated genes in the $Braf^{fl/+}$ group. These genes participate in the formation and maintenance of tight junctions, adherent junctions, and other intercellular connections between endothelial cells, which are crucial for maintaining the stability and integrity of the vascular wall [48–54]. Actually, a series of in vitro or in vivo studies have corroborated the changes in cytoskeletal proteins revealed by our data [12, 13, 59]. The activation of MAPK signaling could regulate cell volume and actin dynamics, leading to a significant increase in the volume of these endothelial cells. Moreover, even in the absence of migration signals, these cells exhibit high migratory capabilities. These results indicated that the pathophysiological mechanisms revealed by the *Braf* mouse model may be extrapolated to sporadic BAVMs with

other mutations. However, the current literature lacks sufficient data to establish a definitive conclusion regarding the genotype-phenotype correlations of BAVMs. Therefore, we believe that further investigations involving comprehensive clinical data and animal models are warranted to elucidate the potential discrepancies associated with different mutations (such as *KRAS* and *BRAF*) or distinct mutation sites within the same gene (e.g., *KRAS*$^{p.G12A}$, *KRAS*$^{p.G12D}$, and *KRAS*$^{p.G12V}$).

The challenges associated with invasive treatment of BAVMs made pharmacologic therapy an appealing avenue for further investigation. Isolated cases of refractory extracranial AVMs have demonstrated that trametinib, a MAP2K1 inhibitor, could attenuate arteriovenous shunt flow and alleviate symptoms including pain, ulceration, and most notably, bleeding [60]. However, the lack of available data currently impedes the assessment of the efficacy of MAPK inhibition therapy for BAVMs. Given the favorable clinical similarities observed in the current BAVM model, its therapeutic outcome can serve as a reliable indicator for human BAVMs. In our investigation, we noticed that early administration of Dabrafenib significantly inhibited the formation of BAVMs; however, the therapeutic efficacy was diminished if the BAVM lesions had already been established. Considering that the BAVMs of clinical patients may have formed years previously, these findings may suggest an unfavorable clinical efficacy of MAPK signaling targeted therapy for BAVMs. A plausible explanation is that the activation of MAPK signaling is essential for initial vascular dilation; however, once arteriovenous shunts have been established, the role of MAPK activation in subsequent AVM progression may be superseded by robust blood flow. However, it should be noted that the current findings lack sufficient data to assess the potential of inhibiting the *RAS-RAF-MEK-ERK* pathway for stabilizing AVM lesions by inducing effects such as reducing the hemorrhagic rate of BAVMs, even if there is no change in lesion size. Therefore, further studies specifically tailored for this field should be anticipated.

Taken together, our findings demonstrated that sporadic BAVM can be induced by focal intracerebral injection of AAV-BR1-*Cre* in mice harboring the lox-stop-lox *Braf*^{V600E} genetic variant. This model closely resembled the clinical manifestations of sporadic BAVMs in humans. We identified that the dilation of preexisting microvasculature may be the primary process contributing to BAVM formation. Target therapy demonstrated significant efficacy in impeding this pathogenic process during its early stages; however, it may be ineffective for established BAVMs. Ongoing research using this BAVM animal model would provide new insights into the pathophysiology of sporadic BAVMs and contribute to the development of novel treatment strategies.

Data availability No datasets were generated or analysed during the current study.

Declarations

Data sharing statement The authors confirmed that all the data that supported the conclusions of this study have been included in the main article and its supplementary material. Additional data derived from this study, which also supported the presented findings, can be obtained by contacting the corresponding authors.

Consent to participate Informed consent was obtained from all individual participants included in the study.

Competing interests The authors declare no competing interests.

References

1. Solomon RA, Connolly ES Jr (2017) Arteriovenous malformations of the brain. N Engl J Med 376(19):1859–1866. https://doi.org/10.1056/NEJMra1607407
2. Hong T, Yan Y, Li J, Radovanovic I, Ma X, Shao YW, Yu J, Ma Y, Zhang P, Ling F, Huang S, Zhang H, Wang Y (2019) High prevalence of KRAS/BRAF somatic mutations in brain and spinal cord arteriovenous malformations. Brain 142(1):23–34. https://doi.org/10.1093/brain/awy307
3. Stapf C, Labovitz DL, Sciacca RR, Mast H, Mohr JP, Sacco RL (2002) Incidence of adult brain arteriovenous malformation hemorrhage in a prospective population-based stroke survey. Cerebrovasc Dis 13(1):43–46. https://doi.org/10.1159/000047745
4. van Beijnum J, van der Worp HB, Buis DR, Al-Shahi Salman R, Kappelle LJ, Rinkel GJ, van der Sprenkel JW, Vandertop WP, Algra A, Klijn CJ (2011) Treatment of brain arteriovenous malformations: a systematic review and meta-analysis. JAMA 306(18):2011–2019. https://doi.org/10.1001/jama.2011.1632
5. Raper DMS, Winkler EA, Rutledge WC, Cooke DL, Abla AA (2020) An update on medications for brain arteriovenous

malformations. Neurosurgery 87(5):871–878. https://doi.org/10.1093/neuros/nyaa192

6. Crist AM, Zhou X, Garai J, Lee AR, Thoele J, Ullmer C, Klein C, Zabaleta J, Meadows SM (2019) Angiopoietin-2 inhibition rescues arteriovenous malformation in a Smad4 Hereditary Hemorrhagic Telangiectasia Mouse Model. Circulation 139(17):2049–2063. https://doi.org/10.1161/CIRCULATIONAHA.118.036952

7. Han C, Lang MJ, Nguyen CL, Luna Melendez E, Mehta S, Turner GH, Lawton MT, Oh SP (2021) Novel experimental model of brain arteriovenous malformations using conditional Alk1 gene deletion in transgenic mice. J Neurosurg 1–12. https://doi.org/10.3171/2021.6.JNS21717

8. Ola R, Kunzel SH, Zhang F, Genet G, Chakraborty R, Pibouin-Fragner L, Martin K, Sessa W, Dubrac A, Eichmann A (2018) SMAD4 prevents Flow Induced Arteriovenous malformations by inhibiting casein kinase 2. Circulation 138(21):2379–2394. https://doi.org/10.1161/CIRCULATIONAHA.118.033842

9. Bharatha A, Faughnan ME, Kim H, Pourmohamad T, Krings T, Bayrak-Toydemir P, Pawlikowska L, McCulloch CE, Lawton MT, Dowd CF, Young WL, Terbrugge KG (2012) Brain arteriovenous malformation multiplicity predicts the diagnosis of hereditary hemorrhagic telangiectasia: quantitative assessment. Stroke 43(1):72–78. https://doi.org/10.1161/STROKEAHA.111.629865

10. Yang W, Liu A, Hung AL, Braileanu M, Wang JY, Caplan JM, Colby GP, Coon AL, Tamargo RJ, Ahn ES, Huang J (2016) Lower risk of intracranial arteriovenous malformation hemorrhage in patients with Hereditary Hemorrhagic Telangiectasia. Neurosurgery 78(5):684–693. https://doi.org/10.1227/NEU.0000000000001103

11. Al-Olabi L, Polubothu S, Dowsett K, Andrews KA, Stadnik P, Joseph AP, Knox R, Pittman A, Clark G, Baird W, Bulstrode N, Glover M, Gordon K, Hargrave D, Huson SM, Jacques TS, James G, Kondolf H, Kangesu L, Keppler-Noreuil KM, Khan A, Lindhurst MJ, Lipson M, Mansour S, O'Hara J, Mahon C, Mosica A, Moss C, Murthy A, Ong J, Parker VE, Riviere JB, Sapp JC, Sebire NJ, Shah R, Sivakumar B, Thomas A, Virasami A, Waelchli R, Zeng Z, Biesecker LG, Barnacle A, Topf M, Semple RK, Patton EE, Kinsler VA (2018) Mosaic RAS/MAPK variants cause sporadic vascular malformations which respond to targeted therapy. J Clin Invest 128(4):1496–1508. https://doi.org/10.1172/JCI98589

12. Nikolaev SI, Vetiska S, Bonilla X, Boudreau E, Jauhiainen S, Rezai Jahromi B, Khyzha N, DiStefano PV, Suutarinen S, Kiehl TR, Mendes Pereira V, Herman AM, Krings T, Andrade-Barazarte H, Tung T, Valiante T, Zadeh G, Tymianski M, Rauramaa T, Yla-Herttuala S, Wythe JD, Antonarakis SE, Frosen J, Fish JE, Radovanovic I (2018) Somatic activating KRAS mutations in arteriovenous malformations of the brain. N Engl J Med 378(3):250–261. https://doi.org/10.1056/NEJMoa1709449

13. Park ES, Kim S, Huang S, Yoo JY, Korbelin J, Lee TJ, Kaur B, Dash PK, Chen PR, Kim E (2021) Selective endothelial hyperactivation of oncogenic KRAS induces brain arteriovenous malformations in mice. Ann Neurol 89(5):926–941. https://doi.org/10.1002/ana.26059

14. Scherschinski L, Han C, Kim YH, Winkler EA, Catapano JS, Schriber TD, Vajkoczy P, Lawton MT, Oh SP (2023) Localized conditional induction of brain arteriovenous malformations in a mouse model of hereditary hemorrhagic telangiectasia. Angiogenesis. https://doi.org/10.1007/s10456-023-09881-w

15. Dankort D, Filenova E, Collado M, Serrano M, Jones K, McMahon M (2007) A new mouse model to explore the initiation, progression, and therapy of BRAFV600E-induced lung tumors. Genes Dev 21(4):379–384. https://doi.org/10.1101/gad.1516407

16. Fish JE, Flores Suarez CP, Boudreau E, Herman AM, Gutierrez MC, Gustafson D, DiStefano PV, Cui M, Chen Z, De Ruiz KB, Schexnayder TS, Ward CS, Radovanovic I, Wythe JD (2020) Somatic gain of KRAS function in the endothelium is sufficient

to cause vascular malformations that require MEK but not PI3K signaling. Circ Res 127(6):727–743. https://doi.org/10.1161/CIRCRESAHA.119.316500

17. Ren AA, Snellings DA, Su YS, Hong CC, Castro M, Tang AT, Detter MR, Hobson N, Girard R, Romanos S, Lightle R, Moore T, Shenkar R, Benavides C, Beaman MM, Muller-Fielitz H, Chen M, Mericko P, Yang J, Sung DC, Lawton MT, Ruppert JM, Schwaninger M, Korbelin J, Potente M, Awad IA, Marchuk DA, Kahn ML (2021) PIK3CA and CCM mutations fuel cavernomas through a cancer-like mechanism. Nature 594(7862):271–276. https://doi.org/10.1038/s41586-021-03562-8

18. Qiu B, Zhao Z, Wang N, Feng Z, Chen XJ, Chen W, Sun W, Ge WP, Wang Y (2023) A systematic observation of vasodynamics from different segments along the cerebral vasculature in the penumbra zone of awake mice following cerebral ischemia and recanalization. J Cereb Blood Flow Metab 43(5):665–679. https://doi.org/10.1177/0271678X221146128

19. Ren J, Huang Y, Ren Y, Tu T, Qiu B, Ai D, Bi Z, Bai X, Li F, Li JL, Chen XJ, Feng Z, Guo Z, Lei J, Tian A, Cui Z, Lindner V, Adams RH, Wang Y, Zhao F, Korbelin J, Sun W, Wang Y, Zhang H, Hong T, Ge WP (2023) Somatic variants of MAP3K3 are sufficient to cause cerebral and spinal cord cavernous malformations. Brain. https://doi.org/10.1093/brain/awad104

20. Peng J, Pang J, Huang L, Enkhjargal B, Zhang T, Mo J, Wu P, Xu W, Zuo Y, Peng J, Zuo G, Chen L, Tang J, Zhang JH, Jiang Y (2019) LRP1 activation attenuates white matter injury by modulating microglial polarization through Shc1/PI3K/Akt pathway after subarachnoid hemorrhage in rats. Redox Biol 21:101121. https://doi.org/10.1016/j.redox.2019.101121

21. Smith LK, Parmenter T, Kleinschmidt M, Kusnadi EP, Kang J, Martin CA, Lau P, Patel R, Lorent J, Papadopoli D, Trigos A, Ward T, Rao AD, Lelliott EJ, Sheppard KE, Goode D, Hicks RJ, Tiganis T, Simpson KJ, Larsson O, Blythe B, Cullinane C, Wickramasinghe VO, Pearson RB, McArthur GA (2022) Adaptive translational reprogramming of metabolism limits the response to targeted therapy in BRAF(V600) melanoma. Nat Commun 13(1):1100. https://doi.org/10.1038/s41467-022-28705-x

22. Tu T, Yin S, Pang J, Zhang X, Zhang L, Zhang Y, Xie Y, Guo K, Chen L, Peng J, Jiang Y (2021) Irisin contributes to Neuroprotection by promoting mitochondrial Biogenesis after experimental subarachnoid hemorrhage. Front Aging Neurosci 13:640215. https://doi.org/10.3389/fnagi.2021.640215

23. Yang X, Dai Z, Gao C, Yin Y, Shi C, Liu R, Zhuge Q, Huang Y, Zhou B, Han Z, Zheng X (2022) Cerebral cavernous malformation development in chronic mouse models driven by dual recombinases induced gene deletion in brain endothelial cells. J Cereb Blood Flow Metab 42(12):2230–2244. https://doi.org/10.1177/0271678X221105995

24. Lu Y, Dai Y, Ou S, Miao Y, Wang Y, Liu Q, Wang Y, Wei P, Shan Y, Zhao G (2022) Using a bipolar electrode to create a temporal lobe Epilepsy Mouse Model by Electrical Kindling of the Amygdala. J Vis Exp 184. https://doi.org/10.3791/64113

25. Racine RJ (1972) Modification of seizure activity by electrical stimulation. II. Motor seizure. Electroencephalogr Clin Neurophysiol 32(3):281–294. https://doi.org/10.1016/0013-4694(72)90177-0

26. Liew JA, Yang W, Mashouf LA, Li S, Caplan JM, Tamargo RJ, Huang J (2020) Incidence of spontaneous obliteration of untreated brain arteriovenous malformations. Neurosurgery 86(1):139–149. https://doi.org/10.1093/neuros/nyz047

27. Chen CJ, Ding D, Derdeyn CP, Lanzino G, Friedlander RM, Southerland AM, Lawton MT, Sheehan JP (2020) Brain arteriovenous malformations: a review of natural history, pathobiology, and interventions. Neurology 95(20):917–927. https://doi.org/10.1212/WNL.0000000000010968

28. Sun Z, Kemp SS, Lin PK, Aguera KN, Davis GE (2022) Endothelial k-RasV12 expression induces Capillary Deficiency attributable

to marked Tube Network expansion coupled to reduced pericytes and basement membranes. Arterioscler Thromb Vasc Biol 42(2):205–222. https://doi.org/10.1161/ATVBAHA.121.316798

29. Zhang H, Peng H, Yan D, Wang K, Yuan K, Chen Y, Li Z, Li R, Li R, Lu J, Chen X, Ye X, Wang H, Zhao Y, Hao Q (2023) The micro-pathological characteristics in cerebral arteriovenous malformations(cAVMs). Microvasc Res 145:104452. https://doi.org/10.1016/j.mvr.2022.104452

30. Winkler EA, Birk H, Burkhardt JK, Chen X, Yue JK, Guo D, Rutledge WC, Lasker GF, Partow C, Tihan T, Chang EF, Su H, Kim H, Walcott BP, Lawton MT (2018) Reductions in brain pericytes are associated with arteriovenous malformation vascular instability. J Neurosurg 129(6):1464–1474. https://doi.org/10.3171/2017.6.JNS17860

31. Tu J, Stoodley MA, Morgan MK, Storer KP (2006) Ultrastructure of perinidal capillaries in cerebral arteriovenous malformations. Neurosurgery 58(5):961–970 discussion 961–970. https://doi.org/10.1227/01.NEU.0000210248.39504.B5

32. Rustenhoven J, Tanumihardja C, Kipnis J (2021) Cerebrovascular anomalies: perspectives from Immunology and Cerebrospinal Fluid Flow. Circ Res 129(1):174–194. https://doi.org/10.1161/CIRCRESAHA.121.318173

33. Winkler EA, Kim CN, Ross JM, Garcia JH, Gil E, Oh I, Chen LQ, Wu D, Catapano JS, Raygor K, Narsinh K, Kim H, Weinsheimer S, Cooke DL, Walcott BP, Lawton MT, Gupta N, Zlokovic BV, Chang EF, Abla AA, Lim DA, Nowakowski TJ (2022) A single-cell atlas of the normal and malformed human brain vasculature. Science 375(6584):eabi7377. https://doi.org/10.1126/science.abi7377

34. Kalucka J, de Rooij L, Goveia J, Rohlenova K, Dumas SJ, Meta E, Conchinha NV, Taverna F, Teuwen LA, Veys K, Garcia-Caballero M, Khan S, Geldhof V, Sokol L, Chen R, Treps L, Borri M, de Zeeuw P, Dubois C, Karakach TK, Falkenberg KD, Parys M, Yin X, Vinckier S, Du Y, Fenton RA, Schoonjans L, Dewerchin M, Eelen G, Thienpont B, Lin L, Bolund L, Li X, Luo Y, Carmeliet P (2020) Single-cell transcriptome atlas of murine endothelial cells. Cell 180(4):764–779e720. https://doi.org/10.1016/j.cell.2020.01.015

35. Judith D, Versapuech M, Bejjani F, Palaric M, Verlhac P, Kuster A, Lepont L, Gallois-Montbrun S, Janvier K, Berlioz-Torrent C (2023) ATG5 selectively engages virus-tethered BST2/tetherin in an LC3C-associated pathway. Proc Natl Acad Sci U S A 120(20):e2217451120. https://doi.org/10.1073/pnas.2217451120

36. Kong N, Shan T, Wang H, Jiao Y, Zuo Y, Li L, Tong W, Yu L, Jiang Y, Zhou Y, Li G, Gao F, Yu H, Zheng H, Tong G (2020) BST2 suppresses porcine epidemic diarrhea virus replication by targeting and degrading virus nucleocapsid protein with selective autophagy. Autophagy 16(10):1737–1752. https://doi.org/10.1080/15548627.2019.1707487

37. Sun X, Zeng H, Kumar A, Belser JA, Maines TR, Tumpey TM (2016) Constitutively expressed IFITM3 protein in human endothelial cells poses an early infection block to human influenza viruses. J Virol 90(24):11157–11167. https://doi.org/10.1128/JVI.01254-16

38. Hur JY, Frost GR, Wu X, Crump C, Pan SJ, Wong E, Barros M, Li T, Nie P, Zhai Y, Wang JC, Tcw J, Guo L, McKenzie A, Ming C, Zhou X, Wang M, Sagi Y, Renton AE, Esposito BT, Kim Y, Sadleir KR, Trinh I, Rissman RA, Vassar R, Zhang B, Johnson DS, Masliah E, Greengard P, Goate A, Li YM (2020) The innate immunity protein IFITM3 modulates gamma-secretase in Alzheimer's disease. Nature 586(7831):735–740. https://doi.org/10.1038/s41586-020-2681-2

39. Malik MNH, Waqas SF, Zeitvogel J, Cheng J, Geffers R, Gouda ZA, Elsaman AM, Radwan AR, Schefzyk M, Braubach P, Auber B, Olmer R, Musken M, Roesner LM, Gerold G, Schuchardt S, Merkert S, Martin U, Meissner F, Werfel T, Pessler F (2022) Congenital deficiency reveals critical role of ISG15 in skin homeostasis. J Clin Invest 132(3). https://doi.org/10.1172/JCI141573

40. Colonne PM, Sahni A, Sahni SK (2011) Rickettsia conorii infection stimulates the expression of ISG15 and ISG15 protease UBP43 in human microvascular endothelial cells. Biochem Biophys Res Commun 416(1–2):153–158. https://doi.org/10.1016/j.bbrc.2011.11.015

41. Zhang W, Li Y, Xin S, Yang L, Jiang M, Xin Y, Wang Y, Cao P, Zhang S, Yang Y, Lu J (2023) The emerging roles of IFIT3 in antiviral innate immunity and cellular biology. J Med Virol 95(1):e28259. https://doi.org/10.1002/jmv.28259

42. Choi YJ, Bowman JW, Jung JU (2018) A talented duo: IFIT1 and IFIT3 Patrol viral RNA caps. Immunity 48(3):474–476. https://doi.org/10.1016/j.immuni.2018.03.001

43. Lupieri A, Smirnova NF, Solinhac R, Malet N, Benamar M, Saoudi A, Santos-Zas I, Zeboudj L, Ait-Oufella H, Hirsch E, Ohayon P, Lhermusier T, Carrie D, Arnal JF, Ramel D, Gayral S, Laffargue M (2020) Smooth muscle cells-derived CXCL10 prevents endothelial healing through PI3Kgamma-dependent T cells response. Cardiovasc Res 116(2):438–449. https://doi.org/10.1093/cvr/cvz122

44. Secchiero P, Corallini F, di Iasio MG, Gonelli A, Barbarotto E, Zauli G (2005) TRAIL counteracts the proadhesive activity of inflammatory cytokines in endothelial cells by down-modulating CCL8 and CXCL10 chemokine expression and release. Blood 105(9):3413–3419. https://doi.org/10.1182/blood-2004-10-4111

45. Pollard TD, Cooper JA (2009) Actin, a central player in cell shape and movement. Science 326(5957):1208–1212. https://doi.org/10.1126/science.1175862

46. Gudimchuk NB, McIntosh JR (2021) Regulation of microtubule dynamics, mechanics and function through the growing tip. Nat Rev Mol Cell Biol 22(12):777–795. https://doi.org/10.1038/s41580-021-00399-x

47. Lechler T, Mapelli M (2021) Spindle positioning and its impact on vertebrate tissue architecture and cell fate. Nat Rev Mol Cell Biol 22(10):691–708. https://doi.org/10.1038/s41580-021-00384-4

48. Niziol M, Zinczuk J, Zareba K, Guzinska-Ustymowicz K, Pryczynicz A (2021) Immunohistochemical analysis of the expression of adhesion proteins: TNS1, TNS2 and TNS3 in correlation with clinicopathological parameters in gastric Cancer. Biomolecules 11(5). https://doi.org/10.3390/biom11050640

49. Lee YJ, Yamada S, Lo SH (2023) Phase transition of tensin-1 during the focal adhesion disassembly and cell division. Proc Natl Acad Sci U S A 120(15):e2303037120. https://doi.org/10.1073/pnas.2303037120

50. Balbuena P, Li W, Ehrich M (2011) Assessments of tight junction proteins occludin, claudin 5 and scaffold proteins ZO1 and ZO2 in endothelial cells of the rat blood-brain barrier: cellular responses to neurotoxicants malathion and lead acetate. Neurotoxicology 32(1):58–67. https://doi.org/10.1016/j.neuro.2010.10.004

51. Xu J, Kausalya PJ, Van Hul N, Caldez MJ, Xu S, Ong AGM, Woo WL, Mohamed Ali S, Kaldis P, Hunziker W (2021) Protective functions of ZO-2/Tjp2 expressed in Hepatocytes and Cholangiocytes Against Liver Injury and Cholestasis. Gastroenterology 160(6):2103–2118. https://doi.org/10.1053/j.gastro.2021.01.027

52. Kotelevets L, Chastre E (2021) A New Story of the three magi: scaffolding proteins and lncRNA suppressors of Cancer. Cancers (Basel) 13(17). https://doi.org/10.3390/cancers13174264

53. Tsukita S, Furuse M (1999) Occludin and claudins in tight-junction strands: leading or supporting players? Trends Cell Biol 9(7):268–273. https://doi.org/10.1016/s0962-8924(99)01578-0

54. Chen F, Ohashi N, Li W, Eckman C, Nguyen JH (2009) Disruptions of occludin and claudin-5 in brain endothelial cells in vitro and in brains of mice with acute liver failure. Hepatology 50(6):1914–1923. https://doi.org/10.1002/hep.23203

55. Jarvelin P, Wright R, Pekonen H, Keranen S, Rauramaa T, Frosen J (2020) Histopathology of brain AVMs part I: microhemorrhages and changes in the nidal vessels. Acta Neurochir (Wien) 162(7):1735–1740. https://doi.org/10.1007/s00701-020-04391-w

56. Wright R, Jarvelin P, Pekonen H, Keranen S, Rauramaa T, Frosen J (2020) Histopathology of brain AVMs part II: inflammation in arteriovenous malformation of the brain. Acta Neurochir (Wien) 162(7):1741–1747. https://doi.org/10.1007/s00701-020-04328-3

57. Sandalcioglu IE, Wende D, Eggert A, Muller D, Roggenbuck U, Gasser T, Wiedemayer H, Stolke D (2006) Vascular endothelial growth factor plasma levels are significantly elevated in patients with cerebral arteriovenous malformations. Cerebrovasc Dis 21(3):154–158. https://doi.org/10.1159/000090526

58. Kciuk M, Gielecinska A, Budzinska A, Mojzych M, Kontek R (2022) Metastasis and MAPK pathways. Int J Mol Sci 23(7). https://doi.org/10.3390/ijms23073847

59. Murphy PA, Kim TN, Huang L, Nielsen CM, Lawton MT, Adams RH, Schaffer CB, Wang RA (2014) Constitutively active Notch4 receptor elicits brain arteriovenous malformations through enlargement of capillary-like vessels. Proc Natl Acad Sci U S A 111(50):18007–18012. https://doi.org/10.1073/pnas.1415316111

60. Boon LM, Dekeuleneer V, Coulie J, Marot L, Bataille AC, Hammer F, Clapuyt P, Jeanjean A, Dompmartin A, Miikka Vikkula M Case report study of thalidomide therapy in 18 patients with severe arteriovenous malformations. Nat Cardiovasc Res 1, 562–567. https://doi.org/10.1038/s44161-022-00080-2